

Journal of Materials Chemistry B

Accepted Manuscript



This article can be cited before page numbers have been issued, to do this please use: Z. Xie, D. Wang, T. Fan, C. Xing, Z. Li, W. Tao, L. Liu, S. bao, D. Fan and H. Zhang, *J. Mater. Chem. B*, 2018, DOI: 10.1039/C8TB00729B.



This is an Accepted Manuscript, which has been through the Royal Society of Chemistry peer review process and has been accepted for publication.

Accepted Manuscripts are published online shortly after acceptance, before technical editing, formatting and proof reading. Using this free service, authors can make their results available to the community, in citable form, before we publish the edited article. We will replace this Accepted Manuscript with the edited and formatted Advance Article as soon as it is available.

You can find more information about Accepted Manuscripts in the [author guidelines](#).

Please note that technical editing may introduce minor changes to the text and/or graphics, which may alter content. The journal's standard [Terms & Conditions](#) and the ethical guidelines, outlined in our [author and reviewer resource centre](#), still apply. In no event shall the Royal Society of Chemistry be held responsible for any errors or omissions in this Accepted Manuscript or any consequences arising from the use of any information it contains.



ARTICLE

Black Phosphorus analogue Tin Sulfide Nanosheets: Synthesis and Application as Near-Infrared Photothermal Agents and Drug Delivery Platforms for Cancer Therapy

Received 00th January 20xx,
Accepted 00th January 20xx

DOI: 10.1039/x0xx00000x

www.rsc.org/

Zhongjian Xie ^{a,1}, Dou Wang ^{b,c,1}, Taojian Fan ^{a1}, Chenyang Xing ^a, Zhongjun Li ^a, Wei Tao ^{d,*}, Liping Liu ^{b,*}, Shiyun Bao ^{b,*}, Dianyan Fan ^a, and Han Zhang ^{a,*}

Two-dimensional (2D) inorganic nanomaterials for biomedical application still face the challenge of simultaneously offering a high photothermal conversion efficiency (PTCE), efficient drug delivery, biocompatibility and biodegradability. Herein, cancer treatment using a tin sulfide nanosheets (SnS NSs) based dual therapy nano-platform (SDTNP), including photothermal- and chemo-therapy, is demonstrated. SnS, a black phosphorus (BP) analogue binary IV–VI compound, was synthesized using liquid phase exfoliation. SnS NSs comprising 2–4 layers exhibited good biocompatibility and a high PTCE of 39.3 %, which is higher than other popular 2D materials. The SnS NSs showed a stable photothermal performance over 2 h of laser irradiation and exhibited ~14 % degradation after 10 h of irradiation. It was also found that SnS NSs show high loading of small molecules such as doxorubicin (DOX) (up to ~200 % in weight). Consequently, the SDTNP achieved notable tumor therapy through the combination of photothermal- and chemo-therapy both *in vitro* and *in vivo*. Our study may pave the way for the biomedical application of SnS and other IV–VI compound-based 2D nanomaterials. Compared with traditional therapies, SnS NSs based laser therapy is green and efficient, due to its biocompatibility, photo-degradability, high efficiency photothermal properties and high drug loading.

1. Introduction

Since the discovery of single-layer graphene in 2004,¹ significant effort has been devoted to exploring new two-dimensional (2D) nanomaterials (NMs) with useful physicochemical properties; such as transition metal dichalcogenides (TMDs),² metal-organic frameworks (MOFs),³ hexagonal boron nitride (hBN),⁴ covalent-organic frameworks (COFs),⁵ layered dual hydroxides (LDHs)⁶ and black phosphorus (BP).^{7–11} These materials have various applications in optoelectronics, energy storage and conversion, and biomedicine.

Photothermal therapy (PTT), a therapeutic strategy in which light energy is converted into heat, has been widely studied in effective cancer therapy. Due to the minimal invasiveness and high selectivity of light irradiation, PTT is considered a promising alternative to conventional clinical cancer treatments, for example surgery, radiotherapy, and chemotherapy. In addition to well-known photothermal converters, such as noble metal nanoparticles,^{12,13} and carbon nanotubes,¹⁴ 2D NMs have emerged as an important family of potential photothermal converters, as demonstrated in several reports on graphene oxide (GO),¹⁵ MoS₂,¹⁶ BP,¹⁷ palladium metal (Pd),¹⁸ and antimonene quantum dots (AMQDs).¹⁹

Ti₃C₂ MXenes were recently reported as an effective photothermal agent under sun irradiation.²⁰ The ultrathin Ti₃C₂ MXenes showed strong optical absorption in the NIR region with an extinction coefficient as high as 29.1 Lg⁻¹cm⁻¹.²¹ It was demonstrated for highly effective photothermal ablation of tumors.²² Although the high PTT performance of Ti₃C₂ MXenes, its fabrication is still a problem with hazardous and time-consuming process using HF pretreatment. Fortunately, a simple fluorine-free fabrication method was proposed to solve this problem.²³ Besides the Ti₃C₂ MXenes, another newly developed Nb₂C MXenes exhibited high photothermal conversion efficiency (36.4% at 808 nm and 45.65% at 1064 nm). The Nb₂C MXene intrinsically features unique enzyme-responsive biodegradability and high biocompatibility. Importantly, the surface-engineered Nb₂C MXene present

^aShenzhen Engineering Laboratory of Phosphorene and Optoelectronics and Key Laboratory of Optoelectronic Devices and Systems of Ministry of Education and Guangdong Province, Shenzhen University, Shenzhen 518060, China.

^{*}To whom correspondence should be addressed.

E-mail: h Zhang@szu.edu.cn

^bDepartment of Hepatobiliary and Pancreatic Surgery, the 2nd Clinical medicine College (Shenzhen People's Hospital) of Jinan University, Shenzhen 518020, China.

E-mail: baomi94@163.com; leoliping@aliyun.com

^cIntegrated Chinese and Western Medicine Postdoctoral research station, Jinan University, Guangzhou 510632, China

^dCenter for Nanomedicine and Department of Anesthesiology, Brigham and Women's Hospital, Harvard Medical School, Boston, MA, USA.

E-mail: wtao@bwh.harvard.edu

¹Z. Xie, D. Wang and T. Fan contributed equally to this work.

Electronic Supplementary Information (ESI) available: [The stability of SnS NSs; Fluorescence of FITC and DOX; Photodynamic study of SnS NSs]. See DOI: 10.1039/x0xx00000x

highly efficient *in vivo* photothermal ablation of tumor.²⁴ For *in vivo* theranostic, the Ta₄C₃ MXenes exhibit unique dual-mode photoacoustic/computed tomography imaging and are highly effective for *in vivo* photothermal ablation of tumors.²⁵

BP has also recently attracted significant attention. It has a layer-dependent band gap of 0.3–2 eV, highly accurate optical response, and anisotropic charge transport, resulting in interesting electronic and photoelectronic applications.^{26–28} Recently, several studies have shown the potential of BP NMs in biomedical applications. BP quantum dots, BP nanoparticles and even BP nanosheet-based hybrid aerogels, have been shown to be efficient NIR photothermal agents.^{8,17,29,30} Moreover, the potential of using a BP-based theranostic delivery platform has also been demonstrated.¹⁰ It has a high drug loading capacity because of its atomically thin 2D structure, and relatively large surface area owing to its wrinkled topography.^{31,32}

Tin sulfide (SnS), a BP analogue binary IV–VI compound, not only crystallizes in layered structures via van der Waals forces, but also has a similar wrinkled structure to BP.³³ SnS exhibits strong anisotropic optoelectronic and mechanical properties,^{34–36} as well as dual indirect and direct band gaps. The indirect band gap of SnS varies from 1.07 to 1.25 eV and the direct band gap varies from 1.30 to 1.39 eV, which lies in between those of Si (1.12 eV) and GaAs (1.43 eV).³⁶ Correspondingly, it has large absorption coefficients ($>10^4 \text{ cm}^{-1}$) across the ultraviolet, visible, and NIR regions of the spectrum,^{33,37} which are substantially higher than those of materials such as cadmium telluride (CdTe), copper indium selenide (CIS) and copper indium gallium selenide (CIGS).³⁶ In contrast to the scarcity of In and Ga, the constituent elements of SnS are relatively abundant. And compared with the toxicity of Cd and Se, Sn and S are safer for the environment. Therefore, the suitable band gap and large absorption coefficient of SnS in the NIR region may satisfy the requisite absorption for NIR photothermal transduction, and its wrinkled structure could lead to a high drug loading ratio similar to BP.^{31,32}

SnS is also biocompatible and relatively stable, which are important attributes in biomedical applications.³⁸ Specifically, tin is one of the microelements necessary for human health, indicating its potential biocompatibility.³⁹ Inorganic tin compounds are poorly absorbed by the human body and are rapidly excreted in faeces, which accounts for their low toxicity.⁴⁰ Human volunteers showed mild signs of tin toxicity when given a high concentration dose of 1400 mg L^{-1} .⁴⁰ Interestingly, long-term animal carcinogenic studies showed fewer malignant tumors in animals exposed to tin than in controls.⁴⁰ Furthermore, a tin compound exhibited interesting anti-proliferative behavior in human ovarian tumors.⁴¹ More recently, it has been reported that nanoparticles with greater density achieve more efficient passive tumor targeting and longer retention times in highly permeable organs.⁴² The density of SnS is higher than some typical 2D materials, such as BP, graphene and MoS₂, which may result in SnS showing more efficient tumor targeting and longer retention times.

Currently, few photothermal agents simultaneously meet the requirements of a suitable absorption spectrum in the biological NIR region, high efficiency drug delivery, biodegradability and biocompatibility, outlined above. Therefore, the development of novel theranostic agents combining all of these ideal properties has significant clinical value. Based on the similarity of its properties to BP, SnS warrants investigation of its potential as a photothermal and drug delivery agent. Its physical (suitable band gap, large absorption coefficient in biological NIR region and potential efficient drug loading due to its wrinkled structure) and biological (non-toxic Sn and S elements, potential biocompatibility and potential anti-cancer effect) features show significant promise.

Herein, we designed a dual-function theranostic platform based on the photothermal properties and drug loading potential of 2D SnS NSs (**Figure 1**), and applied this 2D SnS platform in cancer theranostics. SnS NSs were synthesized from bulk SnS using the liquid exfoliation method and were then functionalized with targeting and imaging agents. The functionalized SnS NSs were then used as theranostic agents. The SnS NSs display excellent biocompatibility, while exhibiting efficient photothermal behavior. Furthermore, a high drug loading ratio (DOX/SnS NSs = ~200 % in weight) can be obtained due to its puckered structure. This theranostic platform can achieve both photothermal- and chemo-therapy, and exhibited an enhanced antitumor effect both *in vitro* and *in vivo* without observable side effects or toxicity to healthy tissue. Our study demonstrated the promising application of SnS NSs as an innovative 2D platform for PTT and theranostic delivery in the treatment of tumors. Owing to its promising therapeutic performance and good biocompatibility, we expect to shed new light on IV–VI compounds for their potential in biomedical applications.

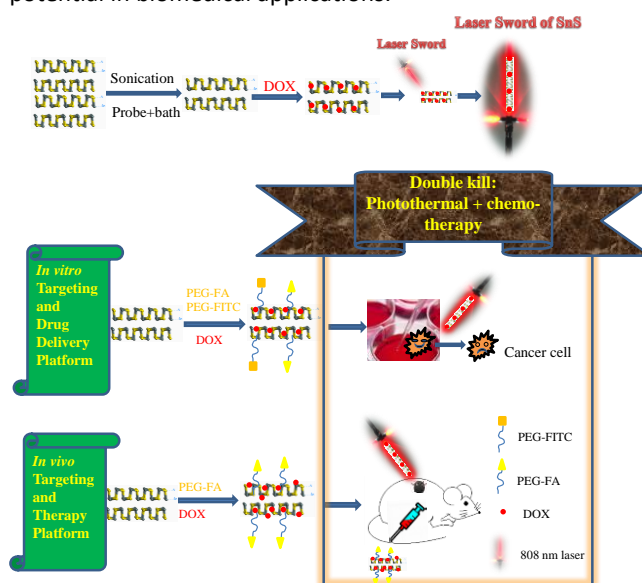


Figure 1. Schematic representation of the SDTNP for *in vitro* and *in vivo* experiments. 1: DOX (therapeutic agent), 2: PEG-FA (targeting agent), 3: PEG-FITC (fluorescent imaging agent).

2. Experimental

2.1. Materials

The bulk SnS was purchased from J&K Scientific. PEG-NH₂, FITC-PEG-NH₂ and FA-PEG-NH₂ were purchased from Nanocs Inc. (New York, USA). The molecular weight (MW) of PEG applied in this study is 2k Da. Phosphate buffered saline (PBS) (pH 7.4), trypsin-EDTA, fetal bovine serum (FBS), DMEM/F12(1:1), RPMI-1640 medium, and penicillin/streptomycin were purchased from Gibco Life Technologies (AG, Switzerland). Doxorubicin hydrochloride, paraformaldehyde, and 4',6-diamidino-2-phenylindole (DAPI) were purchased from Sigma-Aldrich (St. Louis, MO, USA). AO/PI assay kit was obtained from Logos Biosystems. Hypure water (18.25 MΩ.cm, 25 °C) was used to prepare water-based dispersions. All other chemicals used in this work were analytical reagent grade.

2.2. Synthesis of SnS NSs

The SnS NSs were prepared by liquid exfoliation. Briefly, 100 mg of the obtained SnS was added to 50 mL of iso propyle alcohol (IPA). The liquid exfoliation involves probe sonication for 10 h and bath sonication for 10 h. The power of probe sonication is 240 W with the On/Off cycle of 2/4 s. The power of bath sonication is 360 W. Both the temperatures of probe sonication and bath sonication are controlled below room temperature. In order to get the monosized SnS NSs, the range of centrifugation speed was narrowed. Firstly, the centrifugation speed of 4000 rpm was used to remove the large non-exfoliated SnS particles. Then, the supernatant was centrifuged at 6000 rpm and the obtained SnS NSs in the sediment were shown in Figure 2a,b.

2.3. Characterization techniques

Transmission electron microscopy (TEM, JEM1230), atomic force microscopy (AFM, Bruker, Dimension Fastscan) were used to characterize the morphology and height of SnS nanosheets (NSs). To confirm the crystal feature of SnS NSs, high-resolution transmission electron microscopy (HRTEM, Tecnai G2 F30) was used to characterize the crystal lattice and selected-area electron diffraction (SAED) of SnS NSs. For AFM sample, the SnS NSs were dispersed on Si substrate by drop-casting method and the images were scanned at 512 pixels per line. UV-Vis-NIR absorption spectra of SnS NSs were measured in the range of 200-1100 nm with step of 1 nm by using UV-Vis absorbance spectrometer (Cary 60, Agilent). Raman tests were performed on a high-resolution confocal Raman microscope (HORIBA LabRAM HR800) at room temperature. To avoid disturbance, the Raman tests were excited at wavelength of 532 nm and 638 nm, respectively. X-ray diffractometer (XRD, Ultima IV) was used to confirm the crystal structure of SnS NSs.

2.4. Cell culture assays

SMCC-7721 (Human hepatocellular carcinoma), A549 (human lung carcinoma), B16 (Mouse melanoma) and HeLa (Human cervical cancer) cell lines were originally obtained from American Type Culture Collection (ATCC, Rockville, MD). A549, B16 and HeLa cells were cultured in RPMI-1640 medium with 10% FBS and 1% penicillin/streptomycin at 37 °C with 5% CO₂,

SMCC-7721 cells were cultured in DMEM/F12 (1:1) medium in the same condition.

DOI: 10.1039/C8TB00729B

2.5. *In vitro* toxicity

SMCC-7721, A549, B16 and HeLa cells were seeded at a density of 8×10^3 cells /well in 96-well plates and then incubated for 10 h. Afterwards, the cells were incubated with SnS NSs at different SnS NSs concentrations (10, 25, 50, 100 ppm) for 48 h (fresh medium with the same SnS NSs concentrations were changed every day). Three multiple holes were set for every sample. The formulations were changed with CCK-8-contained medium and an additional 90 min-incubation was conducted for the cells. Subsequently, a microplate reader (ELx808, BioTek, USA) was used to measure the absorbance at 450 nm.

2.6. *In vitro* photothermal therapy study

SMCC-7721 cells were incubated with SnS NSs (0, 25, 50 and 100 ppm) for 6 h at 37 °C under the same condition and then irradiated by 808 nm laser for 10 min. For each concentration of SnS NSs, three multiple holes were set. The distance from laser tip to 96-well plates was 0.5 cm. After additional incubation for 12 h, the relative cell viabilities were then measured by the CCK-8 cell cytotoxicity assay. The cell viability was normalized by control sample without treatment.

2.7. *In vitro* chemotherapy study

The SMCC-7721 cells were planted in 96-well plates at a density of 8×10^3 cells per well and incubated for 12 h. Then the culture medium in each well was replaced with 100 μL of SnS (20, 30, 40 ppm), SnS (as PTT group; 20, 30, 40 ppm), SnS-FA (as PTT group; 20, 30, 40 ppm for SnS), SnS-PEG-FA-DOX (as chemotherapy group; 20, 30, 40 ppm for SnS and 10, 15, 20 ppm for DOX), SnS-PEG-FA-DOX (as chemotherapy + PTT group; 20, 30, 40 ppm for SnS and 10, 15, 20 ppm for DOX). After additional incubation for 6 h, the cells in PTT therapy group and chemotherapy + PTT group were irradiated with 808 nm laser for 10 min. After additional incubation for 12 h, the relative cell viabilities were then measured by the CCK-8 cell cytotoxicity assay.

2.8. DAPI staining assay

SMCC-7721 cells were seeded at the density 8×10^3 cells into the 96-well plates and treated with SnS-PEG-FITC and SnS-PEG-FA-FITC for 6 h. SMCC-7721 cells were fixed with 4% paraformaldehyde for 15 minutes and 0.2% Triton x-100 for 20 min, then the cells were stained with 1 μg/mL DAPI for 5 minutes, followed by observation under the fluorescence microscope.

2.9. *In vivo* photothermal assay

Tumor bearing nude mice were injected with 100 μL of SnS NSs (100 ppm). After 1 h injection, the nude mice were irradiated with 808 nm laser at 1 W/cm² for 5 min. During the irradiation process, an IR thermal camera (FLIR E50, USA) was used to monitor the temperature changes of the tumor sites.

2.10. *In vivo* anticancer therapy

Female BALB/c (nu/nu) mice (6 weeks old) used in this research were all purchased from Guangdong Medical Laboratory Animal Center (Guangzhou, China), and all the animal researches were conducted in compliance with the guidelines approved by the Animal Welfare and Research

Ethics Committee at Shenzhen University (ID: 2017003). The tumor model was generated by injecting SMCC-7721 cells (3.5×10^6 per mouse) in the left axilla of each mouse. When the tumor volumes reached about 100 mm^3 , the mice were randomly divided into 5 groups (5 mice for each group). Groups 1-5 were in vein injected with Saline ($200 \mu\text{L}$), SnS (10 mg/kg), SnS-PEG-FA-DOX (10 mg/kg for SnS and 6 mg/kg for DOX), SnS-PEG-FA-DOX (10 mg/kg for SnS and 6 mg/kg for DOX), respectively. The mice in groups 2, 3 and 5 were anesthetized and irradiated with an 808 nm laser at 1 W/cm^2 for 10 min after 12 h injection at tumor site. Subsequently, the body weight and tumor growth were monitored by a balance and caliper every the other day. The tumor volume (V) was calculated according to the formula: $V = 4\pi/3 \times (\text{tumor length}/2) \times (\text{tumor width}/2)^2$. Relative tumor size was calculated as V/V_0 , where V_0 was the initial tumor volume of the treatment. The mice were humanely sacrificed after two weeks of treatment.

2.11. Histology examination

Finally, the mice were euthanized. The heart, liver, spleen, lung, kidney and tumor tissues were sliced and dehydrated successively and embedded in liquid paraffin for hematoxylin and eosin (H&E).

3. Results and discussions

3.1. Characterizations

The SnS NSs used in this study were prepared using a liquid exfoliation method in isopropyl alcohol (IPA). Previous work showed that SnS NSs could be exfoliated using N-methyl-2-pyrrolidone (NMP).³⁷ IPA has a lower boiling point than NMP and can therefore readily substitute it to avoid potential toxicity to healthy tissue.

To obtain SnS NSs with the desired dimensions, dispersions of SnS NSs in IPA at different centrifugal speeds were characterized using transmission electron microscopy (TEM) and atomic force microscopy (AFM). Figure 2a shows the dimensions of the SnS NSs obtained from the supernatant after centrifuging at 5000 rpm . The TEM image shows a typical lateral SnS NS size of less than 50 nm . The AFM image (Figure 2b) shows that the thickness of the SnS NSs falls within the range $4\text{--}8 \text{ nm}$. Clear lattice fringes with inter-atomic d-spacing of 0.29 nm and 0.35 nm for SnS NSs in Figure 2c can be ascribed to the (111) and (120) planes, respectively. Fast Fourier transformation (FFT) of the high-resolution TEM (HRTEM) image demonstrates the crystallinity of the SnS NSs, showing the expected crystallographic lattice reflections. Furthermore, the selected-area electron diffraction (SAED) image in Figure 2d suggests that the highly crystalline features of the SnS NSs were not destroyed during the liquid exfoliation procedure.

The chemical composition and crystal structure of bulk SnS and SnS NSs were characterized using X-ray photoelectron spectroscopy (XPS) and X-ray diffraction (XRD). In Figure 2e, the two strong peaks at 485.7 and 494.2 eV are ascribed to the $3d\ 5/2$ and $3d\ 3/2$ orbitals for both bulk SnS and SnS NSs. No other impurities, such as SnS_2 , Sn or S were detected,

indicating the high purity of the starting material and final exfoliated SnS NSs. The unsymmetrical XPS peak may indicate the impurity of SnO. As shown in Figure S1 (Supporting Information), both the bulk SnS and exfoliated SnS NSs exhibited typical crystalline diffraction.

The bulk SnS and exfoliated SnS NSs were also characterized by Raman spectroscopy (Figure 2f). For bulk SnS, three distinct peaks were observed in the range $100\text{--}500 \text{ cm}^{-1}$. The peak at 165.7 cm^{-1} corresponds to the B_{3g} mode, and the Raman peaks at 190.3 and 218.2 cm^{-1} can be assigned to the Ag mode.^{43,44} For exfoliated SnS NSs, three similar peaks were observed at 167 , 193.3 and 220.7 cm^{-1} , respectively. This indicates a Raman shift for the exfoliated SnS NSs compared with the bulk SnS. It can be concluded that, of the two vibrational modes, the Ag mode is more sensitive to the thickness of the SnS NS layers. All characterizations confirm the purity and crystallinity of the exfoliated SnS NSs. Consequently, the as prepared SnS NSs with relatively small size ($<50 \text{ nm}$) could be useful in biomedical applications.

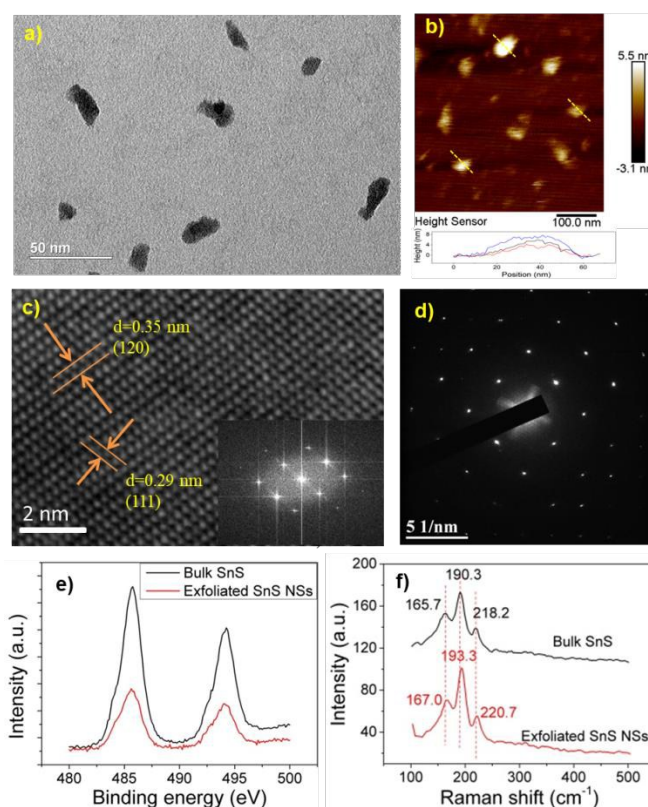


Figure 2. Typical characterization of SnS NSs, including TEM, AFM, HRTEM, XPS and Raman spectroscopy. a) TEM image of SnS NSs and b) corresponding AFM image. c) Crystal lattice shown by HRTEM and corresponding fast Fourier transformation (FFT). d) Crystalline features shown by selected-area electron diffraction (SAED). e) XPS curves of bulk and exfoliated SnS NSs. f) Raman spectra of bulk and exfoliated SnS NSs.

3.2. Photothermal response

The stability of the SnS NSs in deionized water was characterized over ten days. After this time the absorbance of

the SnS NSs showed a slight decrease, which indicated that the SnS NSs were stable for at least ten days following synthesis (Figure S2). Although the SnS NSs did not degrade obviously when dispersed in water, aggregation of the NSs in physiological medium is a further concern. Therefore, the stability of the SnS NSs in physiological medium was also characterized. It was found that the SnS NSs readily aggregated in the presence of salts when dispersed in phosphate buffered saline (PBS) (Figure 3b). Positively charged monofunctional poly(ethylene glycol) amine (PEG-NH₂) was thus used to coat the surface of the SnS NSs by electrostatic adsorption to give SnS-PEG NSs. The success of this coating was validated by STEM-EDS, which showed the co-localization of four different elements; Sn and S from the SnS NSs, and N and O from the surface coating of PEG-NH₂ (Figure 3a). After surface modification, the zeta potential of the SnS NSs changed from -23 to -15 mV. Figure 3b showed the coating halo of PEG on SnS NSs. Even after the coating, it can be observed that the size of SnS NSs were ~50 nm, which was favorable for bio-experiments. Consequently, the SnS-PEG NSs exhibited enhanced stability in PBS (Figure 3c, d). The surface coating of FITC-PEG-FA on SnS NSs was further confirmed by absorbance (Figure S4).

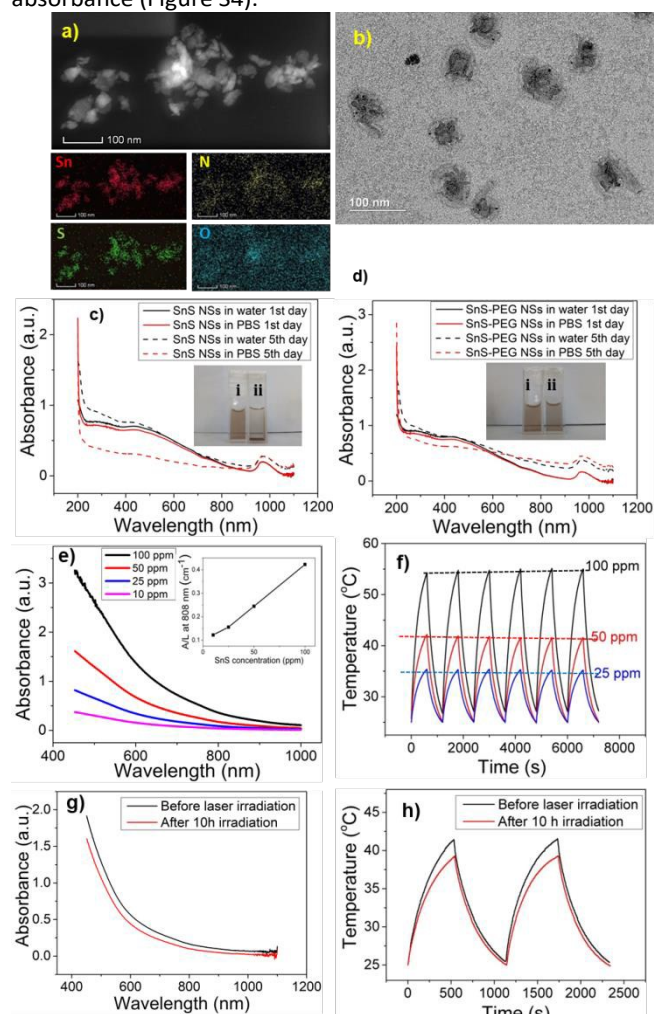


Figure 3. a) Scanning transmission electron microscopy (STEM) with energy dispersive X-ray spectroscopy (EDS) mapping of

SnS-PEG NSs. b) PEG coating of SnS NSs shown by TEM image. The absorbance of c) SnS NSs and d) SnS-PEG NSs in deionized water and PBS for 0 day and 5th day, respectively. The insets show the photographs of SnS NSs and SnS-PEG NSs on 5th day dispersed (i) in deionized water and (ii) in PBS. e) Absorption spectra of SnS NSs dispersed in water at different concentrations. The inset shows the normalized absorbance intensity divided by the characteristic length of the cuvette (A/L) at different concentrations for $\lambda=808$ nm. f) Photothermal heating curves of SnS NSs dispersed in water at different concentrations under irradiation with an 808 nm laser for six cycles. The dotted lines show the relatively stable photothermal temperature change of SnS NSs. g) Degradation of absorbance after 10 h of laser irradiation. h) The degradation of photothermal temperature change corresponding to the degradation of absorbance in g).

The optical absorption spectra of SnS NSs dispersed in water are shown in Figure 3e. They show a broad absorption band spanning the UV and NIR regions, and are similar to those of other 2D NMs, such as GO⁴⁵, WS₂⁴⁶ and BP.⁸ The concentration (C) of the SnS NSs was determined using inductively coupled plasma atomic emission spectroscopy (ICP-AES). The normalized absorbance over the characteristic length of the cuvette (A/L , where A is absorbance and L is light path) at 808 nm for different concentrations of SnS NSs, could be determined (Figure 3e). The extinction coefficient at 808 nm was estimated to be $3.4 \text{ L g}^{-1} \text{ cm}^{-1}$, according to the Lambert-Beer law ($A/L=kC$, where k is extinction coefficient).

The photothermal properties of the SnS NSs were further evaluated. Different concentrations of SnS NSs suspended in water were exposed to an 808 nm NIR laser (power density: 2.0 W cm^{-1}) and the temperature of the suspension was measured as a function of time (Figure 3f). At an SnS concentration of 100 ppm, the temperature increased from 25 °C to 54 °C after 600 s' irradiation, indicating that the SnS NSs can efficiently convert NIR light into thermal energy. Furthermore, by using a reported method,⁴⁷ the photothermal conversion efficiency of the SnS NSs was determined to be 39.3 % (Figure S6), higher than popular photothermal agents, such as copper selenide (22 %), Au nanoparticles (21 %),^{48,49} and black phosphorus quantum dots (BPQDs, 28.4 %),⁸ but lower than MoS₂ (53.3%).⁵⁰

The photothermal stability of the SnS NSs was examined further. Figure 3f shows six photothermal cycles for different SnS NSs concentrations. One photothermal cycle consisted of sample irradiation using an 808 nm laser for 10 min, followed by a further 10 min period with the laser turned off. It was found that the temperature initially increased and then decreased to room temperature by natural cooling. The highest photothermal temperature throughout the six cycles was approximately consistent, shown by the dotted line. This indicated that the SnS NSs did not appreciably deteriorate under NIR irradiation. For the 100 ppm sample, it can be observed that there was a slight increase of ΔT as irradiation cycle number increased, which was due to the increasing concentration of the SnS NSs with the evaporation of the

water dispersant. For the 50 and 25 ppm samples, there was a slight decrease of the highest temperature as irradiation cycle number increased, which may be due to the degradation of the SnS NSs under the laser irradiation. To confirm this hypothesis, the 50 ppm sample was irradiated for a further 10 h. After 10 h of irradiation, both the absorbance and ΔT decreased by $\sim 14\%$, showing the photodegradability of the SnS NSs (Figure 3g, h). This can also be proved by the Raman spectra (Figure S3). When irradiated the laser with strong power, a new phase of SnS_2 appeared.

Based on these observations, it can be concluded that the SnS NSs have good photostability under several hours laser irradiation despite being ultimately photodegradable. This slow degradation profile could make SnS NSs a promising material for PTT.

3.3. Drug delivery platform

2D nanomaterials have been widely used as drug carriers in view of their relatively large surface areas, for example the reported GO ,⁵¹ MoS_2 ⁵² and BP materials.¹⁰ In the present study, the as-prepared SnS NSs were employed as carriers for DOX, a prevalent anti-cancer drug in clinical application.

To load DOX onto SnS NSs, a dispersion of SnS NSs was mixed with DOX at different DOX/SnS NSs feeding ratios and then stirred. To characterize the drug loading process, UV-Vis and fluorescence spectra were measured after stirring for 0, 9 and 24 h. As shown in Figure 4a, the absorbance peaks at ~ 490 nm were attributed to DOX. It was found that the UV-Vis absorbance decreased significantly from 0 h to 9 h due to enclosure of DOX onto the SnS NSs. The spectra then remained essentially stable from 9 h to 24 h, indicating that drug loading was almost complete after 9 h. For absorbance spectra, base lines were built at the DOX peak (black dotted line). The decrease in absorbance was mainly exhibited by the angular rotation of the base line (Figure 4a). The vertical distance from the DOX absorbance peak to the base line was defined as the peak height. The peak heights for 0 h (Peak 1) and 9 h (Peak 2, Figure 4a) were the same, despite having different base lines. Moreover, the spectrum at 9 h was same to that of pure DOX at the same concentration. This indicates that drug loading process decreases the absorbance of SnS NSs but not that of DOX. The loading process of naked SnS NSs and SnS-PEG NSs was almost the same (Figure S7), indicating the PEG coating does not influence the drug loading of SnS NSs.

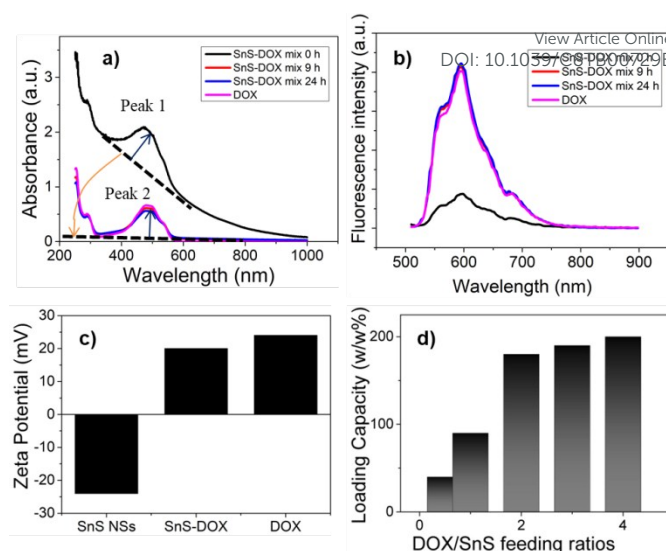


Figure 4. a) UV-Vis absorption and b) fluorescence spectra of DOX and SnS NSs mixed with DOX at $t = 0, 9$ and 24 h. c) Zeta potential of SnS NSs, SnS-DOX and DOX. d) DOX loading capacity of SnS NSs at various DOX/SnS NSs feeding ratios.

Sample fluorescence was measured at the same time points. Fluorescence was measured immediately upon mixing of the SnS NSs and DOX. Compared with pure DOX (same concentration), significant fluorescence quenching at ~ 600 nm was observed. This was due to the strong absorption of SnS NSs at ~ 600 nm. After stirring for 9 h, a marked increase in fluorescence was observed that was same to that of pure DOX at the same concentration. Based on these absorbance and fluorescence observations, it can be reasonably hypothesized that when SnS NSs was DOX loaded the absorbance of SnS NSs decayed and the fluorescence of DOX could be released.

Furthermore, the successful drug loading can be characterized by zeta potential measurement. It was found that the SnS NSs have a negative potential while they became positive when loading DOX (Figure 4c). It also confirms the interaction between SnS NSs and DOX is electrostatic absorption. The drug-loading ratio of the SnS NSs was measured using dialysis method. The SnS NSs and DOX mixture was stirred for 24 h and then dialyzed against deionized water. Free DOX was dialyzed into the water and its concentration can be determined using the normalized absorbance or fluorescence spectra (Figure S6). Our testing conditions showed that the saturation of DOX loading can be up to $\sim 200\%$ (Figure 4d).

As a BP-analogue material, the photothermal performance of SnS is compared with BP. The extinction coefficient ($3.4 \text{ L g}^{-1} \text{ cm}^{-1}$) of SnS is lower than BP⁸ ($14.8 \text{ L g}^{-1} \text{ cm}^{-1}$) but both the drug loading ratio ($\sim 200\%$) and PTCE (39.3%) of SnS are higher than BP (drug loading ratio $\sim 108\%$ ¹⁰ and PTCE of 28.4% ⁸). Moreover, the cost of SnS is much lower than BP, indicating its promising potential in clinical application.

3.4. In vitro experiments

Nanomaterials used in biomedicine must be sufficiently biocompatible; therefore the cytotoxicity of the PEGylated SnS NSs, namely SnS-PEG NSs, to several types of cells was

therefore examined. The standard Cell Counting Kit-8 (CCK-8) cell cytotoxicity assay was carried out to determine the relative viabilities of A549 (human lung carcinoma cells), Hela (Human cervical cancer cells), B16 (Mouse melanoma cells) and SMCC-7721 (Human hepatocellular carcinoma cells) cells after incubation with the SnS-PEG NSs at different concentrations (10, 25, 50, and 100 ppm) for 48 hours. No obvious cytotoxicity could be observed for the four cell types, even at a concentration of 100 ppm, which can achieve a high photothermal performance. This suggests good biocompatibility and suitability of SnS-PEG NSs for biomedical applications (Figure 5c).

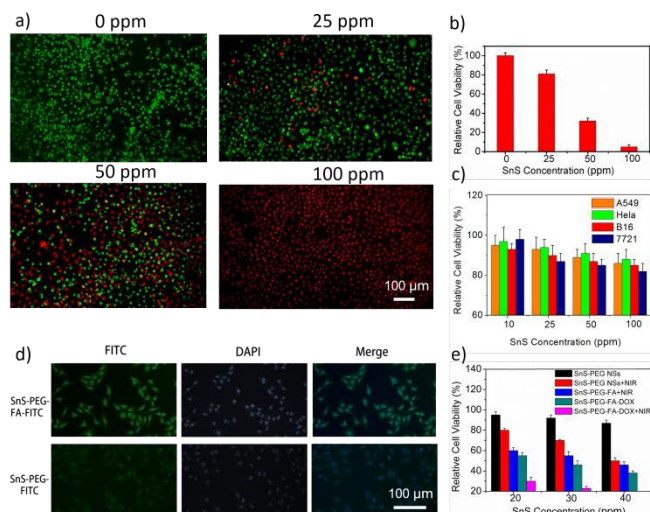


Figure 5. *In vitro* photothermal experiment. a) Photothermal killing effect of SnS-PEG NSs at concentrations of 0, 25, 50 and 100 ppm for SMCC-7721 cancer cells at laser power of 2.0 W cm⁻¹. Fluorescence images of cells stained with acridine orange (green, live cells) and propidium iodide (red, dead cells). b) Relative cell viabilities of SMCC-7721 cells after photothermal killing. c) Relative viabilities of A549, Hela, B16 and SMCC-7721 cells after incubation with various concentrations (10, 25, 50, and 100 ppm) of SnS NSs for 48 h. d) Fluorescence images of SMCC-7721 cancer cells incubated with SnS-PEG-FITC and SnS-PEG-FA-FITC. e) Relative viabilities of SMCC-7721 cells after different treatments at various SnS-PEG NSs concentrations (20, 30, and 40 ppm).

The photothermal killing effect of the SnS-PEG NSs in cancer cells was then investigated. SMCC-7721 cancer cells were incubated with the SnS-PEG NSs for 6 h, and the cells were irradiated with an NIR laser of 808 nm for 10 min. The live/dead cells were differentiated using acridine orange (AO, live cells, green fluorescence) and propidium iodide (PI, dead cells, red fluorescence) co-staining after the PTT. A SnS-PEG NSs-dose-dependent photothermal killing effect was observed for SMCC-7721 cells (Figure 5a). It should be noted that almost all cells were killed after incubating with 100 ppm of the SnS-PEG NSs and exposure to the NIR laser (Figure 5b). These results clearly demonstrate the photothermal efficiency of the SnS-PEG NSs in promoting cancer cell death. The irradiation conditions were also much less intensive than those adopted with Au nanoshells (40 W cm⁻², 5 min)⁵³ and copper selenide

nanocrystals (33 W cm⁻², 5 min)⁵⁴ for *in vitro* photothermal cell destruction.

DOI: 10.1039/C8TB00729B

To achieve an actively-targeted DOX delivery system, we modified SnS-PEG NSs with FA to give SnS-PEG-FA-DOX, based on the specific binding between FA and the FA receptors⁵⁵ over expressed on SMCC-7721 cancer cells (Figure 5d). The tumor cell killing effect of the SDTNP was then investigated. SMCC-7721 cells were incubated with SnS-PEG NSs, and SnS-PEG-FA-DOX, in the presence and absence of laser irradiation. The CCK-8 and live/dead assays were then performed to evaluate therapeutic efficacy *in vitro* (Figure 5e). For the cells treated with SnS and irradiated with laser light, more than 45 % of cells survived at the 40 ppm concentration. For the cells treated with SnS-PEG-FA-DOX without laser irradiation, 60% were killed. Compared with chemotherapy alone (SnS-PEG-FA-DOX in dark), and PTT with SnS under 808 nm laser irradiation, the combined dual treatment of SDTNP offers the most effective cancer cell killing, nearly all of the cells were killed. This demonstrates the tumor cell killing efficacy of the synergistic photothermal- and chemo-therapy of SDTNP (Figure 5e).

3.5. *In vivo* tumor eradication

Based on the *in vitro* therapeutic effects observed, we carried out an *in vivo* antitumor evaluation to validate the enhanced therapeutic effects of the SDTNP. Firstly, we studied its *in vivo* photo-thermal response. After intratumoral injection of PBS and SnS-PEG NSs respectively, animal NIR images and ΔT were monitored using a thermal camera over a 5 min irradiation period. ΔT of the PBS treated mice was only ~5 °C, while that for the SnS-PEG NSs treated animals was more than 23 °C, reaching more significant temperature rises throughout the irradiation period (Figure 6b and Figure 6c). Based on the *in vivo* photothermal effect, we performed an *in vivo* antitumor evaluation to validate the enhanced therapy of cancer. The SMCC-7721 tumor-bearing nude mice were treated with Group 1: saline (control), Group 2: laser irradiation only, Group 3: SnS-PEG NSs with laser irradiation, Group 4: SnS-PEG-FA-DOX without laser irradiation, Group 5: SnS-PEG-FA-DOX with laser irradiation. The tumor volumes were calculated by measuring width and length every two days. At the end point of the experiment, all nude mice were euthanized and tumors were collected. In line with the results of the tumor growth curve shown in Figure 6d, Group 3 showed decreasing tumor growth indicating the promising application of SnS NSs as photothermal agents. Moreover, a significant therapeutic effect could be found in Group 5, demonstrating that an enhanced antitumor effect could be achieved using the combined therapy strategy of SDTNP. The body weight of the nude mice was not found to be significantly affected by treatment, demonstrating that there were no acute side effects of the combined therapy (Figure 6e). To further evaluate the *in vivo* toxicity of SnS NSs, the major organs of the mice were dissected and stained using hematoxylin and eosin (H&E) for histological analysis. As shown in Figure 6f, the treated mice, which were euthanized two weeks after injection of SnS-PEG-FA-DOX with NIR irradiation, exhibited no

significant damage to the normal tissues, including the heart, liver, spleen, lung, and kidney. This indicates that SDTNP treatment had no observable side effects or toxicity towards healthy tissue.

images of major organs from treated mice as in the conditions of d) and e).

DOI: 10.1039/C8TB00729B

4. Conclusion

In summary, the treatment of cancer cells and tumors using the SDTNP, including photothermal- and chemo-therapy, was demonstrated. While exhibiting excellent biocompatibility, the SDTNP also showed high photothermal performance with photothermal conversion efficiency of 39.3 % at 808 nm. Furthermore, SnS NSs showed stable photothermal performance over short periods of laser irradiation (2 h) whilst demonstrating photodegradability over longer exposure. As a drug carrier, SnS NSs can accommodate a high DOX/SnS NSs ratio of ~200 % (w/w %) due to their wrinkled structure, similar to BP. Consequently, SnS NSs composed of only a few layers can be developed as both a high efficiency and stable photothermal agent, and efficient drug carrier with degradable characteristics.

Furthermore, we demonstrated the efficacy of SDTNP in several carcinoma cell lines as well as in nude mice subcutaneous xenograft tumors. In *in vitro* experiments, SDTNP showed an enhanced therapeutic effect through the combination of photothermal- and chemo-therapy. Moreover, this enhanced therapeutic effect was also demonstrated *in vivo*, and no observable side effects or toxicity was detected in healthy tissue. Consequently, 2D SnS NSs, a BP-analogue binary IV–VI compound, have been demonstrated to be an innovative 2D nano-platform for photothermal therapy and theranostic drug delivery for the treatment of tumors. This may pave the way for the biomedical application of other IV–VI compounds, such as GeS and SnSe, due to their low cost and biocompatibility.

Compared with traditional treatments, this dual therapy nano-platform based on SnS NSs is a green and efficient approach, using low power laser radiation due to its safety, limited side effects and no trauma; and using SnS NSs due to their high efficiency photothermal and drug loading features, and photodegradability. Its clinical application could have a significant effect on the future treatment of cancer.

Conclusions

The conclusions section should come in this section at the end of the article, before the acknowledgements.

Conflicts of interest

There are no conflicts of interest to declare

Acknowledgements

The research is partially supported by the National Natural Science Fund (Grant Nos. 61435010, 61575089 and 81470868), Science and Technology Innovation Commission of Shenzhen (KQTD2015032416270385 and JCYJ20150625103619275), the Science and Technology Planning Project of Guangdong

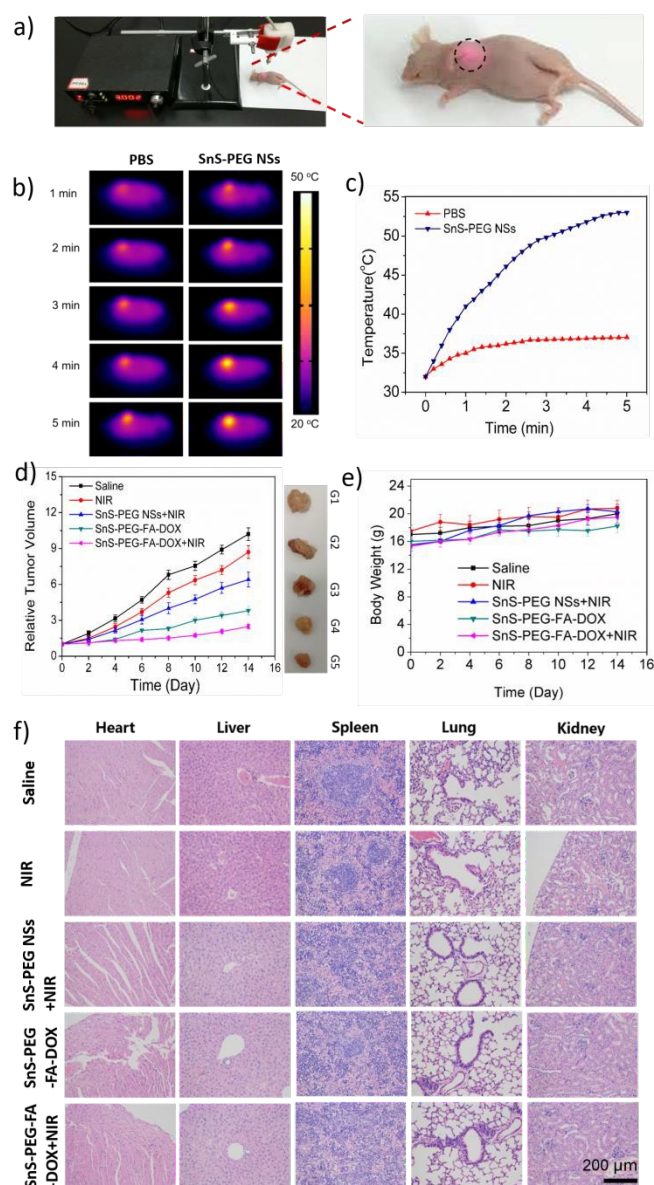


Figure 6. *In vivo* imaging and antitumor effect of SDTNP. a) Photograph of nude mice with 808 nm laser irradiation. b) Thermal images of mice bearing tumors with injection of SnS NSs and exposure to 808 nm laser irradiation (1.0 W cm^{-2} , 5 min). c) The change of SMCC-7721 tumor temperature in mice during laser irradiation as indicated in b). d) Corresponding growth curves and representative photographs of tumors removed from the euthanized nude mice treated with saline solution, laser irradiation only, SnS with laser irradiation, SnS-PEG-FA-DOX without laser irradiation and SnS-PEG-FA-DOX with laser irradiation. The relative tumor volumes were normalized to their initial size. e) Body weight of nude mice taken every other day after various treatments. f) H&E stained

Province (Grant No. 2016B050501005), the Educational Commission of Guangdong Province (Grant No. 2016KCXTD006) and China Postdoctoral Science Foundation (Grant No. 2017M612730). We thank Sarah Dodds, PhD, from Liwen Bianji, Edanz Editing China (www.liwenbianji.cn/ac), for editing the English text of a draft of this manuscript.

Notes and references

- 1 K. S. Novoselov, A. K. Geim, S. V. Morozov, D. Jiang, Y. Zhang, S. V. Dubonos, I. V. Grigorieva and A. A. Firsov, *Science*, 2004, **306**, 666–669.
- 2 Q. H. Wang, K. Kalantarzadeh, A. Kis, J. N. Coleman and M. S. Strano, *Nat. Nanotechnol.*, 2012, **7**, 699–712.
- 3 K. Sumida, D. L. Rogow, J. A. Mason, T. M. McDonald, E. D. Bloch, Z. R. Herm, T. H. Bae and J. R. Long, *Chem. Rev.*, 2017, **112**, 724–781.
- 4 J. Xue, J. Sanchez-Yamagishi, D. Bulmash, P. Jacquod, A. Deshpande, K. Watanabe, T. Taniguchi, P. Jarillo-Herrero and B. J. Leroy, *Nat. Mater.*, 2011, **10**, 282–285.
- 5 H. Xu, J. Gao and D. Jiang, *Nat. Chem.*, 2015, **7**, 905.
- 6 A. I. Khan and D. O'Hare, *Cheminform*, 2002, **12**, 3191–3198.
- 7 H. Wang, X. Yang, W. Shao, S. Chen, J. Xie, X. Zhang, J. Wang and Y. Xie, *J. Am. Chem. Soc.*, 2015, **137**, 11376–11382.
- 8 Z. Sun, H. Xie, S. Tang, Y. XF, Z. Guo, J. Shao, H. Zhang, H. Huang, H. Wang and C. PK, *Angew. Chemie*, 2015, **54**, 11526.
- 9 L. Li, Y. Yu, G. Ye, Q. Ge, X. Ou, H. Wu, D. Feng, X. Chen and Y. Zhang, *Nat. Nanotechnol.*, 2014, **9**, 372–377.
- 10 W. Tao, X. Zhu, X. Yu, X. Zeng, Q. Xiao, X. Zhang, X. Ji, X. Wang, J. Shi, H. Zhang and L. Mei, *Adv. Mater.*, 2017, **29**, 1–9.
- 11 W. Chen, J. Ouyang, H. Liu, M. Chen, K. Zeng, J. Sheng, Z. Liu, Y. Han, L. Wang, J. Li, L. Deng, Y. N. Liu and S. Guo, *Adv. Mater.*, 2017, **29**, 1–7.
- 12 Z. Qin and J. C. Bischof, *Chem. Soc. Rev.*, 2012, **41**, 1191–1217.
- 13 R. Bardhan, S. Lal, A. Joshi and N. J. Halas, *Acc. Chem. Res.*, 2011, **44**, 936–946.
- 14 C. Liang, S. Diao, C. Wang, H. Gong, T. Liu, G. Hong, X. Shi, H. Dai and Z. Liu, *Adv. Mater.*, 2014, **26**, 5646–5652.
- 15 M. Li, X. Yang, J. Ren, K. Qu and X. Qu, *Adv. Mater.*, 2012, **24**, 1621.
- 16 S. S. Chou, B. Kaehr, J. Kim, B. M. Foley, M. De, P. E. Hopkins, J. Huang, C. J. Brinker and V. P. Dravid, *Angew. Chemie*, 2013, **52**, 4160–4164.
- 17 J. Shao, H. Xie, H. Huang, Z. Li, Z. Sun, Y. Xu, Q. Xiao, X. F. Yu, Y. Zhao and H. Zhang, *Nat. Commun.*, 2016, **7**, 12967.
- 18 X. Huang, S. Tang, B. Liu, B. Ren and N. Zheng, *Adv. Mater.*, 2011, **23**, 3420.
- 19 W. Tao, X. Ji, X. Xu, M. A. Islam, Z. Li, S. Chen, P. E. Saw, H. Zhang, Z. Bharwani, Z. Guo, J. Shi and O. C. Farokhzad, *Angew. Chemie*, 2017, **100**, 49, 11896–11900.
- 20 R. Li, L. Zhang, L. Shi and P. Wang, *ACS Nano*, 2017, **11**, 3752–3759.
- 21 J. Xuan, Z. Wang, Y. Chen, D. Liang, L. Cheng, X. Yang, Z. Liu, R. Ma, T. Sasaki and F. Geng, *Angew. Chemie*, 2016, **55**, 14569.
- 22 H. Lin, X. Wang, L. Yu, Y. Chen and J. Shi, *Nano Lett.*, 2017, **17**, 384.
- 23 Y. Chen, C. Tan, H. Zhang and L. Wang, *Chem. Soc. Rev.*, 2015, **44**, 2681.
- 24 H. Lin, S. Gao, C. Dai, Y. Chen and J. Shi, *J. Am. Chem. Soc.*, 2017, **139**, 16235–16247.
- 25 H. Lin, Y. Wang, S. Gao, Y. Chen and J. Shi, *Adv. Mater.*, 2018, **30**, 1–11.
- 26 F. Xia, H. Wang and Y. Jia, *Nat. Commun.*, 2014, **5**, 4458.
- 27 A. Castellanosgomez, L. Vicarelli, E. Prada, J. O. Island, K. L. Narasimhaacharya, S. I. Blanter, D. J. Groenendijk, M. Buscema, G. A. Steele and J. V. Alvarez, *2d Mater.*, 2014, **1**, 25001.
- 28 X. Ling, H. Wang, S. Huang, F. Xia and M. S. Dresselhaus, *Proc. Natl. Acad. Sci. U. S. A.*, 2015, **112**, 4523–4530.
- 29 C. Sun, L. Wen, J. Zeng, Y. Wang, Q. Sun, L. Deng, C. Zhao and Z. Li, *Biomaterials*, 2016, **91**, 81.
- 30 C. Xing, G. Jing, X. Liang, M. Qiu, Z. Li, R. Cao, X. Li, D. Fan and H. Zhang, *Nanoscale*, 2017, **9**, 8096–8101.
- 31 J. Kim, S. S. Baik, S. H. Ryu, Y. Sohn, S. Park, B.-G. Park, J. Denlinger, Y. Yi, H. J. Choi and K. S. Kim, *Science*, 2015, **349**, 723–726.
- 32 J. W. Jiang, *Nanotechnology*, 2015, **26**, 365702.
- 33 C. Xin, J. Zheng, Y. Su, S. Li, B. Zhang, Y. Feng and F. Pan, *J. Phys. Chem. C*, 2016, **120**, 22663–22669.
- 34 S. M. Herron, J. T. Tanskanen, K. E. Roelofs and S. F. Bent, *Chem. Mater.*, 2014, **26**, 7106–7113.
- 35 R. E. Banai, L. A. Burton, S. G. Choi, F. Hofherr, T. Sorgenfrei, A. Walsh, B. To, A. Cröll and J. R. S. Brownson, *J. Appl. Phys.*, 2014, **116**, 7363.
- 36 N. K. Reddy, M. Devika and E. S. R. Gopal, *Crit. Rev. Solid State Mater. Sci.*, 2015, **40**, 1–40.
- 37 J. R. Brent, D. J. Lewis, T. Lorenz, E. A. Lewis, N. Savjani, S. J. Haigh, G. Seifert, B. Derby and P. O'Brien, *J. Am. Chem. Soc.*, 2015, **137**, 12689.
- 38 D. Avellaneda, M. T. S. Nair and P. K. Nair, *Thin Solid Films*, 2009, **517**, 2500–2502.
- 39 S. V. De Azevedo, F. R. Moreira and R. C. Campos, *Clin. Biochem.*, 2013, **46**, 123.
- 40 K. A. Winship, *Advers. Drug React. Acute Poisoning Rev.*, 1988, **7**, 19–38.
- 41 M. Cagnoli, A. Alama, F. Barbieri, F. Novelli, C. Bruzzo and F. Sparatore, *Anticancer. Drugs*, 1998, **9**, 603.
- 42 S. Tang, C. Peng, J. Xu, B. Du, Q. Wang, R. D. V. Iii, M. Yu, M. J. Kim and J. Zheng, *Angew. Chemie*, 2016, **128**, 16039–16043.
- 43 J. Chao, Z. Wang, X. Xu, Q. Xiang, W. Song, G. Chen, J. Hu and D. Chen, *Rsc Adv.*, 2012, **3**, 2746–2753.
- 44 A. M. Tripathi and S. Mitra, *Rsc Adv.*, 2014, **4**, 10358–10366.
- 45 J. T. Robinson, S. M. Tabakman, Y. Liang, H. Wang, H. S. Casalongue, D. Vinh and H. Dai, *J. Am. Chem. Soc.*, 2011, **133**, 6825–6831.

ARTICLE

Journal Name

- 46 L. Cheng, J. Liu, X. Gu, H. Gong, X. Shi, T. Liu, C. Wang, X. Wang, G. Liu and H. Xing, *Adv. Mater.*, 2014, **26**, 1886–1893.
- 47 D. K. Roper, W. Ahn and M. Hoepfner, *J. Phys. Chem. C Nanomater. Interfaces*, 2007, **111**, 3636.
- 48 B. Wang, J. H. Wang, Q. Liu, H. Huang, M. Chen, K. Li, C. Li, X. F. Yu and P. K. Chu, *Biomaterials*, 2014, **35**, 1954–1966.
- 49 C. M. Hessel, V. P. Pattani, M. Rasch, M. G. Panthani, B. Koo, J. W. Tunnell and B. A. Korgel, *Nano Lett.*, 2011, **11**, 2560–2566.
- 50 Z. Huang, Y. Qi, D. Yu and J. Zhan, *Rsc Adv.*, 2016, **6**, 31031–31036.
- 51 Z. Liu, J. T. Robinson, X. Sun and H. Dai, *J. Am. Chem. Soc.*, 2008, **130**, 10876–10877.
- 52 T. Liu, C. Wang, X. Gu, H. Gong, L. Cheng, X. Shi, L. Feng, B. Sun and Z. Liu, *Adv. Mater.*, 2014, **26**, 3433–3440.
- 53 M. P. Melancon, W. Lu, Z. Yang, R. Zhang, Z. Cheng, A. M. Elliot, J. Stafford, T. Olson, J. Z. Zhang and C. Li, *Mol. Cancer Ther.*, 2008, **7**, 1730.
- 54 C. M. Hessel, V. P. Pattani, M. Rasch, M. G. Panthani, B. Koo, J. W. Tunnell and B. A. Korgel, *Nano Lett.*, 2011, **11**, 2560.
- 55 W. Tao, J. Zhang, X. Zeng, D. Liu, G. Liu, X. Zhu, Y. Liu, Q. Yu, L. Huang and L. Mei, *Adv. Healthc. Mater.*, 2015, **4**, 1203–1214.

View Article Online
DOI: 10.1039/C8TB00729B

Black Phosphorus analogue Tin Sulfide Nanosheets as Photothermal and Drug Delivery Agents with High Drug Loading Capacity for Cancer Therapy

